# In-Orbit Geometric Calibration for Long-Linear-Array and Wide-Swath Whisk-Broom TIS of SDGSAT-1

Xiaoyan Li, Liyuan Li, Lixing Zhao, Jingjie Jiao, Linyi Jiang, Lan Yang, Fansheng Chen, Senior *Member, IEEE*, and Shengli Sun

***Abstract*— Because of the imaging mechanism complexity of long-linear-array and wide-swath whisk-broom thermal infrared spectrometer (TIS) of the first Sustainable Development Goals Satellite (SDGSAT-1), how to achieve a high geometric positioning accuracy (GPA) becomes the core factor in subsequent geometric quantitative applications. Here, in this article, a three-step in-orbit geometric calibration (GC) strategy comprising the estimations of exterior orientation parameters (EOPs), interior orientation parameters (IOPs), and scanning compensation parameters (SCPs) is proposed to correct the geo-location displacements for whisk-broom TIS. First, in accordance with the optical-mechanical structure and pinhole imaging theory, we establish the rigorous geometric positioning model (RGPM) of TIS and analyze the error resources term-by-term along the error propagation link elaborately. Second, the corresponding rigorous geometric calibration model (RGCM) is constructed in detail based on the 2-D look-angle model and the generalized bias correction matrix. Especially for eliminating the systematic nonlinear errors in the scanning direction, a fifth-degree polynomial is put forward to be employed to fit and compensate for the angular measurement errors of the scanning mirror. Finally, a three-step estimation method is presented to estimate the calibration parameters with ground control points (GCPs). Experimental results based on the spatial references of Landsat 8 panchromatic images and version 2 of advanced spaceborne thermal emission and reflection radiometer (ASTER) global digital elevation model (GDEM2) show that the GPA of the proposed method in along-track and cross-track directions can be better than 1.0 pixels for all three bands, which makes a great sense for associated geometric measurements.**

***Index Terms*— Geometric calibration (GC), geometric positioning accuracy (GPA), rigorous geometric positioning model (RGPM), Sustainable Development Goals Satellite (SDGSAT-1), whisk-broom.**

Manuscript received 22 February 2023; revised 4 April 2023; accepted 12 April 2023. Date of publication 19 April 2023; date of current version 4 May 2023. This work was supported in part by the Strategic Priority Research Program of the Chinese Academy of Sciences under Grant XDA19010102 and in part by the National Natural Science Foundation of China under Grant 62205083 and Grant 61975222. *(Xiaoyan Li and Liyuan Li contributed equally to this work.) (Corresponding authors: Fansheng Chen; Shengli Sun.)*

Xiaoyan Li is with the Key Laboratory of Intelligent Infrared Perception, Chinese Academy of Sciences, Shanghai 200083, China, and also with the Hangzhou Institute for Advanced Study, University of Chinese Academy of Sciences, Hangzhou 310024, China (e-mail: lixiaoyan@ucas.ac.cn).

Liyuan Li, Linyi Jiang, and Lan Yang are with the Shanghai Institute of Technical Physics, Chinese Academy of Sciences, Shanghai 200083, China, and also with the University of Chinese Academy of Sciences, Beijing 100049, China (e-mail: liliyuan@mail.sitp.ac.cn; lyjiang2020@163.com; yanglan3134@163.com).

Lixing Zhao and Jingjie Jiao are with the Hangzhou Institute for Advanced Study, University of Chinese Academy of Sciences, Hangzhou 310024, China (e-mail: zhaolixing21@mails.ucas.ac.cn; jiaojingjie21@mails.ucas.ac.cn).

Fansheng Chen is with the Key Laboratory of Intelligent Infrared Perception, Chinese Academy of Sciences, Shanghai 200083, China, also with the State Key Laboratory of Infrared Physics, Shanghai Institute of Technical Physics, Chinese Academy of Sciences, Shanghai 200083, China, and also with the Hangzhou Institute for Advanced Study, University of Chinese Academy of Sciences, Hangzhou 310024, China (e-mail: cfs@mail.sitp.ac.cn).

Shengli Sun is with the Key Laboratory of Intelligent Infrared Perception, Chinese Academy of Sciences, Shanghai 200083, China (e-mail: Palm_sun@mail.sitp.ac.cn).

Digital Object Identifier 10.1109/TGRS.2023.3268343

## I. Introduction

THERMAL infrared images (TIRIs) responding to the ambient infrared radiation of 8.0–14.0 $\mu$m are widely applied in many important fields of sea-land temperature retrieval, resources exploration, socioeconomic development assessment, unexpected disaster monitoring, and space-sensitive target detecting [1], [2], [3], [4], [5]. Many of the subtle but crucial occurrences, such as the fine portrayal of human activity traces and the principle mining between economy and spatial pattern of human society, especially in a relatively wide area, however, turns out to be difficult to detect and identify because of the compromise between spatial resolution and the swath of existing payloads. For example, although the push-broom thermal infrared sensor (TIRS) and TIRS-2 aboard Landsat 8 and 9 could achieve accurate retrieval of surface temperature with two obtained TIRIs with a spatial resolution of 100 m and a swath of 185 km [6], [7], it is almost impossible to recognize the thermal emissions associated with human traces due to the coarse resolution. Comparatively, although the advanced push-broom Visual and Infrared Multispectral Imager of Gaofen-5 [8] has the ability to provide a higher spatial resolution of 40 m and more long-wave infrared bands, including 8.01–8.39, 8.42–8.83, 10.30–11.30, and 11.40–12.51 $\mu$m, the narrow swath of 60 km greatly limits its real-time application in the research of spatial pattern and distribution of regional energy thermal emissions in a wide area. Therefore, the emergence of a high-resolution and wide-swath thermal infrared payload is exceedingly imperative for higher precision quantitative applications in revealing the associated mechanism between human socioeconomic development and the global distribution of thermal emissions.

Launched on November 5, 2021, Sustainable Development Goals Satellite (SDGSAT-1), carrying three advanced

TABLE I
MAIN SPECIFICATIONS OF TIS AND SDGSAT-1

| SDGSAT-1 | | TIS | |
|---|---|---|---|
| **Items** | **Indexes** | **Items** | **Indexes** |
| Orbit type | Sun-synchronous | Bands | 8.0-10.5um<br>10.3-11.3um<br>11.5-12.5um |
| Altitude | 505km | Detector scale per module | 512×4×3 |
| Inclination | 97.4° | Pixel size | 30um |
| Descending time | 09:30 | resolution | 30m |
| Orbit period | 94.7mins | swath | 300km |
| Revisit interval | 10.5days | Focal length | 505×(1±5%)mm |
| Eccentricity | 0 | FOV along-track/cross-track | 7.0°/33.1° |
| Life | >3years | Scanning period | 7.48s |

payloads, including a thermal infrared spectrometer (TIS), Glimmer Imager, and Multispectral Imager, is the first global sustainable satellite developed by the Chinese Academic of Sciences to provide full-time collaborative scientific observation data for the research of SDGs indicators characterizing the interaction between humans and nature. SDGSAT-1 operates in a sun-synchronous orbit with an altitude of 505 km, an inclination of 97.4°, and a descending intersection time of 9:00 am. Generally, affected by the optical diffraction limit, it is difficult for space-based thermal infrared payloads to achieve a higher resolution, let alone the wide swath simultaneously. For addressing the contradiction between high resolution and wide swath, the TIS is innovatively designed with a multimodule-spliced multispectral long-linear-detector and a high-precision 1-D scanning mirror to achieve the collection of three TIRIs with a resolution of 30 m and a swath of 300 km at an altitude of 505 km simultaneously. At present, TIS is the civilian thermal infrared optical payloads with the highest resolution in China and meanwhile has the world's highest ratio of swath to resolution. Table I shows the detailed specifications of TIS. Additionally, in order to obtain higher sensitivity, the 195 K all-optical path cryogenic optomechanical technology is adopted for TIS to keep the entire instrument in a low temperature environment. Benefit from the scanning mirror and the satellite agility, TIS has three different observation modes, including the general observation mode, the expansion observation mode for the Arctic and Antarctic areas with side-swing imaging, and the emergency observation mode for sudden events with the attitude maneuver.

It is well known that geometric positioning accuracy (GPA) is one of the most important factors determining the results of subsequent quantitative applications, and in-orbit geometric calibration (GC) is a crucial and universal technology for guaranteeing the GPA [9]. It should be noticed that although the imaging mechanism of TIS is capable of achieving high resolution and wide swath simultaneously, the introduction of scanning mirror, however, leads to an increase in positioning error resources such as the installation and angular measurement errors of the mirror. Meanwhile, the rigorous geometric positioning model (RGPM) of TIS has to contain more parameters and inevitably becomes more complicated to calibrate. In addition, the complex geometry of multimodule-spliced multispectral long-linear-detector also increases the difficulty of in-orbit GC.

## II. LITERATURE REVIEW

In general, the laboratory and in-orbit GC are employed to obtain precise imaging parameters of space-based optical payloads. Laboratory calibration is responsible for the initial imaging geometry alignment of the sensor, including accurate estimations of principle point and distance, distortions, and camera installation matrix, which is usually quoted as the initial condition for in-orbit GC. Up to now, different kinds of methods have been developed and demonstrated for precise estimations in laboratories [10], [11], [12]. Affected by the inevitably introduced errors, such as launch shock, spatial thermal environment changes, stress relief of the assembled instrument, and the jitters of satellite attitudes and platform during practical operation, RGPM of the camera will, however, deviate from the previous calibrated condition in the laboratory, which ultimately results in the diminution of GPA. Therefore, in-orbit GC is always implemented after launch, even mandatorily, in early commission for facilitating the GPA improvement of collected images [9], [13], [14], [15], [16], [17]. Exactly, the exterior orientation parameters (EOPs) and interior orientation parameters (IOPs) determining rigorous orientation geometry in imaging instant are supposed to be estimated accurately with high-precision spatial references, such as the ground control points (GCPs) and observable stars, which are a prerequisite foundation of image registration, stitching, as well as 3-D reconstruction [18], [19], [20].

Summarily, there are two types of in-orbit GC strategies at present: reference-dependent calibration (RDC) and reference-independent calibration (RIC). Especially, RDC usually utilizes accurate spatial references, such as the landmarks, coastline, and GCPs from calibration field or digital orthophoto model (DOM) and digital elevation model (DEM) and the observed stars [9], [12], [21], to determine the GC parameters like IOPs and EOPs of RGPM or the rational polynomial coefficients (RPCs) of rational function model (RFM); this method has been adopted by the majority of current space-based optical payloads [9], [13], [14], [15], [16], [17], [21], [22], [23], [24]. For example, based on numerous GCPs extracted from DOM and DEM, Wang et al. [9], [22] successfully obtained IOPs and EOPs with a stepwise calibration approach for GF-4 and GF-6 cameras. And similar GC was also applied to the cameras of ZY1-02C and ZY-3 [23]. Further, Dong et al. [24] elaborately analyzed the influences of different GCP extraction methods on in-orbit GC results of GF-4. Similarly, Lee and Shin [25] fully estimated the misalignment between the attitude frame and camera frame for Deimos-2 through an automatic GCPs extraction algorithm, and an image division and enhancement method are employed by Zhang et al. [17] to extract more GCPs for in-orbit GC of BNU-1 cameras. Cao et al. [16] proposed an in-orbit GC approach to realize precise multifield calibration without losing the accuracy with GCPs from multiple fields for coastal zone imager of HaiYang-1C; however, affected by cloud coverage and distribution of the permanent calibration

fields, it is generally not easy to ensure the availability of a great number of accurate GCPs in time during the early commission phrase, and more severely, it will be worse in desert and ocean areas. Moreover, the in-orbit GC with GCPs has great trouble in performing the immediate calibration requirements for high-speed target positioning of space-based detecting and tracking cameras. For addressing the problems, the star-based GC is raised to be another substitute without the concerns of clouds, eclipse, and interfering daylight [25]. Based on the star map obtained by the camera and star sensors, Guan et al. [26] developed a camera-star sensor installation calibration method for Luojia 1-01 satellite and achieved an accuracy of less than 800 m. Similarly, Li et al. [21] presented a novel stellar-based geometric positioning method to correct the positioning error deriving from spatial thermal deformation for geostationary optical payloads. Although the star-based calibration method is promising and has some advantages compared with GCPs, it is not always applicable because the star numbers collected are not consistently adequate to estimate the calibration parameters. Thus, for eliminating the heavy dependence on the number of stars, Jiang et al. [27] proposed an in-orbit GC method using the relative motion of stars to estimate the calibration parameters of a geostationary camera.

Differently, with the development of space remote sensing technology, RIC is creatively developed according to the special characteristics of the payloads and satellites, such as the strong agility and geometric constraints of overlapped multiview imaging, to calibrate the associated parameters without spatial references. By agile acquisition modes of auto-reverse and cross imaging of PLEIADES-1A/1B, Greslou et al. [28] and Lebegue et al. [29] estimated the EOPs and IOPs of the payloads based on mutual geometric constraints among overlapped image pairs, and in accordance with simulated cross-image pairs, Pi et al. [30] investigated the theoretical effectiveness of reference-independent GC with the associated constraints and the aided digital surface model (DSM). Meanwhile, the self-constraint of multi-attitude images and the DEM were also used to demonstrate the effectiveness of proposed full-link independent calibration method and the capacity for compensating for the systematic errors [31]. Despite these methods being really innovative and applicable for resolving dependencies on spatial references, it is definitely impractical for the other satellites without excellent agile maneuverability. Additionally, the accuracy and robustness of attitude control during agile imaging could be another challenge in practical applications. Therefore, in order to address the limitation of agility, the relative constraints of overlapped image pairs are constructed through generalized models to calibrate the IOPs of the camera. For example, the generalized distortion model of the WFV camera equipped with GF-1 was calibrated with the corresponding pairs extracted from overlapped images [32]. Yang et al. [15] proposed an integrated geometric self-calibration method with the relative constraints between images of each camera and the intersection constraints of stereo images to calculate the calibration parameters of the stereo cameras of ZiYuan-3; meanwhile, a step-wise block adjustment method was developed to conduct integrated processing of large-scale ZY-3 satellite images without GCPs [33]. Based on the positioning consistency of conjugate points between several overlapped images with small intersection angles, an interior self-calibration method was presented by Jiang et al. [34] to eliminate charge coupled device (CCD) distortions of ZY-02C cameras without using control data. It should be noticed that although the EOPs and IOPs could be calibrated with constructed geometric constraints of the image pairs collected by agile imaging or multiview imaging payloads, the absolute pointing errors of EOPs still need to be eliminated with more or less high-precision GCPs. And moreover, the majority of current RIC methods require precise aided DSM or DEM to solve the unstable iterative calculation and reduce the elevation errors during calibration. In conclusion, the RIC turns out to be in the initial research stage presently, and comparatively, the RDC is still the mainstream method and widely employed for in-orbit GC of optical payloads both at home and abroad.

In this article, we propose a three-step in-orbit GC strategy comprising the estimations of EOPs, IOPs and scanning compensation parameters (SCPs) to correct the geometric positioning error of TIS images. The remainder of this article is organized as follows. First, the related works are briefly introduced in Section II. In Section III, the methodology comprising the establishment of RGPM, in-orbit GC strategy, and the assessment method for TIS is presented in detail. Then, Section IV describes the conducted experimental results. Finally, the conclusions of this article are summarized in Section V.

## III. Methodology

This section describes the in-orbit GC methodology of SDGSAT-1 TIS, primarily including the establishment of RGPM, the proposed in-orbit GC strategy, and the positioning accuracy assessment method.

### A. Establishment of RGPM

The RGPM of TIS, depicting the strict mapping relationship between image coordinates in the pixel coordinate system (PCS) and the corresponding object points in earth centered and earth fixed coordinate system (ECEF), is the foundation of high-precision in-orbit GC.

*1) RGPM of TIS:* As shown in Figs. 1–3, the establishment of RGPM refers to many spatial coordinate systems, including PCS, focal plane coordinate system (FPCS), camera coordinate system (CCS), satellite body coordinate system (SBCS), orbit coordinate system (OCS), earth centered inertial (ECI) coordinate system and ECEF coordinate system. Especially, the splicing direction of the multimodule-spliced long-linear-array detector is coincident with the $x$-axes of FPCS, CCS, and SBCS, as well as the flight direction (along-track) of the satellite, and meanwhile, it is perpendicular to the scanning direction (cross-track) of the scanning mirror. The 1-D scanning mirror with a rotating axis parallel to the $x$-axis of CCS

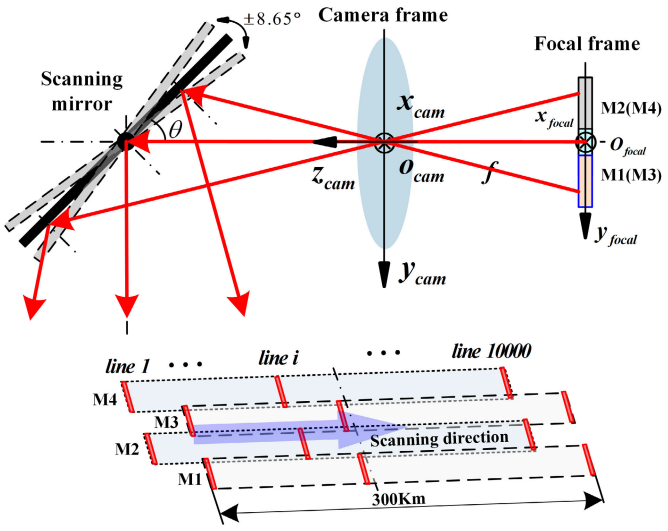


Fig. 1. Diagrams of the imaging geometry of ITS.

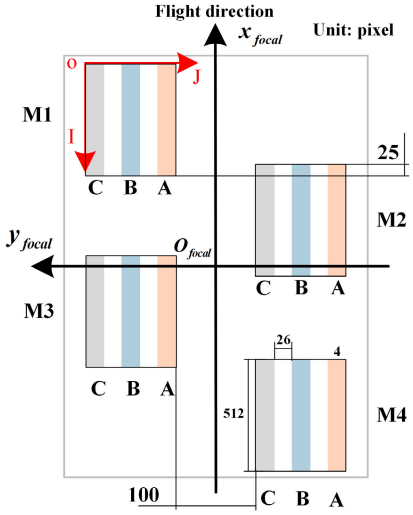


Fig. 2. Layout diagram of the multimodule-spliced long-linear-detector.

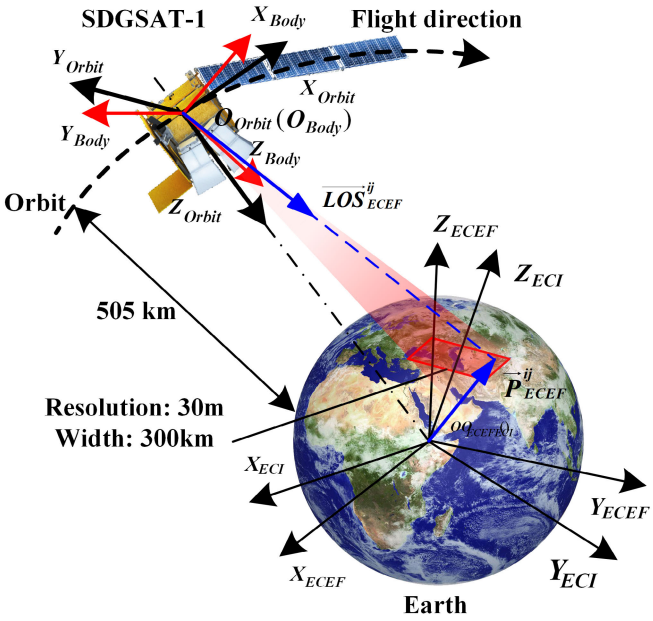


Fig. 3. Schematic of EOM of SDGSAT-1 TIS.

swings forward and backward cross-track in a range of ±8.65° referencing to the initial position to obtain three bands TIRIs with a resolution of 30 m and a swath of 300 km at an altitude of 505 km. The normal scanning mirror in the initial position intersects the optical axis at 45°, and a 2048 × 10 000 image, including four 512 × 10 000 subimages could be collected successfully after each scan. It can be seen that there is a very complicated relative motion comprising of the velocities of the satellite, scanning mirror, and the earth in the imaging instant, which makes it more difficult to obtain a high-precision GPA for TIS. Particularly, the resultant velocities of the forward and backward whisk-broom imaging are really different, resulting in the geometric differences of acquired images.

The RGPM of TIS is comprised of the interior orientation model (IOM) and the exterior orientation model (EOM). As shown in Figs. 1 and 2, IOM describes the geometric transformation relation from image point coordinates in PCS to the unit line-of-sight (LOS) vector in CCS. It can be exactly expressed in the following equation:

$$\overrightarrow{\mathrm{LOS}}_{\mathrm{cam}}^{ij} = R_{\mathrm{ref}}(\theta)\cdot\left\|\begin{bmatrix}\lambda_x & 0 & d_x\\ 0 & \lambda_y & d_y\\ 0 & 0 & -f+\Delta f\end{bmatrix}\begin{bmatrix}j_0-j+\Delta j_0\\ i_0-i+\Delta i_0\\ 1\end{bmatrix}\right\| \tag{1}$$

$$\begin{cases} d_x = -x_0 - \dfrac{\Delta f}{f}x + x\left(k_1r^2+k_2r^4+k_2r^6\right) \\ \qquad + \left[p_1(r^2+2x^2)+2p_2xy\right] + ax + by \\ d_y = -y_0 - \dfrac{\Delta f}{f}y + y\left(k_1r^2+k_2r^4+k_2r^6\right) \\ \qquad + \left[p_2(r^2+2y^2)+2p_1xy\right] \end{cases} \tag{2}$$

where $\overrightarrow{\mathrm{LOS}}_{\mathrm{cam}}^{ij}$ is the exit unit LOS vector corresponding to pixel $(i, j)$ in CCS, $(i, j)$ is the coordinates of the image point in PCS, and $(i_0, j_0)$ and $(\Delta i_0, \Delta j_0)$ are the coordinates and corresponding displacements of the principle point in PCS, respectively. $(\lambda_x, \lambda_y)$ and $(d_x, d_y)$ are the pixel sizes and distortions in the $x$ and $y$ direction of FPCS, and $f$ and $\Delta$f are the principle distance and associated errors in CCS, respectively. $\|P\|$ means the normalization for vector $P$. $R_{\mathrm{ref}}(\theta)$ is the reflect matrix of the scanning mirror, and $\theta$ is the corresponding position angle of the scanning mirror. Equation (2) employed by [11] is employed to represent the distortions of TIS. $(x_0, y_0)$ and $(x, y)$ are the coordinates of the principle point and the image point in FPCS, $r = (x^2 + y^2)^{1/2}$ is the radial distance from $(x, y)$ to principle point in FPCS, $k_1, k_2, k_3$ are the first three coefficients of radial distortion, $p_1$ and $p_2$ are the first two coefficients of decentering distortion, $a$ is a factor for differential scaling, and $b$ describes the axis nonorthogonality in FPCS.

As shown in Fig. 3, the EOM of TIS describes the vector transformation relationship from the exit LOS vector in CCS to the object vector in ECEF. Similarly, it can be expressed in the following equation:

$$\overrightarrow{\mathrm{LOS}}^{ij}_{\mathrm{ECEF}} = R^{\mathrm{ECEF}}_{\mathrm{ECI}}(t) \cdot R^{\mathrm{ECI}}_{\mathrm{Orbit}} \cdot R^{\mathrm{Orbit}}_{\mathrm{Body}}(\text{pitch, roll, yaw}) \cdot R^{\mathrm{Body}}_{\mathrm{cam}}(\alpha, \beta, \gamma) \cdot \overrightarrow{\mathrm{LOS}}^{ij}_{\mathrm{cam}} \quad (3)$$

where $\overrightarrow{\mathrm{LOS}}^{ij}_{\mathrm{cam}}$ is the exit unit vector corresponding to pixel $(i, j)$ in CCS, and $\overrightarrow{\mathrm{LOS}}^{ij}_{\mathrm{ECEF}}$ is the corresponding unit object vector in the ECEF coordinate system. $R^{\mathrm{Body}}_{\mathrm{cam}}$, $R^{\mathrm{Orbit}}_{\mathrm{Body}}$, $R^{\mathrm{ECI}}_{\mathrm{Obit}}$ and $R^{\mathrm{ECEF}}_{\mathrm{ECI}}$ are the transformation matrices from CCS to SBCS, from SBCS to OCS, from OCS to ECI, and from ECI to ECEF, respectively. Especially, $\alpha$, $\beta$, and $\gamma$ are the three installation angles between CCS of TIS and the SBCS of SDGSAT-1, $t$ is the UTC time of imaging instant, which determines the transformation of $R^{\mathrm{ECEF}}_{\mathrm{ECI}}$, and pitch, roll and yaw are the three attitudes angles of the satellite. Generally, the satellite attitudes are measured by star-sensor and gyro in the ECI coordinate system. Therefore, (3) could be simplified as

$$\overrightarrow{\mathrm{LOS}}^{ij}_{\mathrm{ECEF}} = R^{\mathrm{ECEF}}_{\mathrm{ECI}}(t) \cdot R^{\mathrm{ECI}}_{\mathrm{Body}}(\text{pitch, roll, yaw}) \cdot R^{\mathrm{Body}}_{\mathrm{cam}}(\alpha, \beta, \gamma) \cdot \overrightarrow{\mathrm{LOS}}^{ij}_{\mathrm{cam}}. \quad (4)$$

Equations (1) and (4) construct the observation vector of every pixel in obtained images in ECEF. Then it can be seen from Fig. 3 that the LOS vector, the practical position vector of object point, and the position vector of the camera projection center usually being substituted for the satellite position vector constitute a triangle in ECEF. Therefore, the RGPM of TIS could be established strictly as the following:

$$\begin{bmatrix} X^{ij}_{\mathrm{ECEF}} \\ Y^{ij}_{\mathrm{ECEF}} \\ Z^{ij}_{\mathrm{ECEF}} \end{bmatrix} = \begin{bmatrix} X^{\mathrm{sat}}_{\mathrm{ECEF}} \\ Y^{\mathrm{sat}}_{\mathrm{ECEF}} \\ Z^{\mathrm{sat}}_{\mathrm{ECEF}} \end{bmatrix} + \mu \cdot R^{\mathrm{ECEF}}_{\mathrm{ECI}}(t) \cdot R^{\mathrm{ECI}}_{\mathrm{Body}} \cdot R^{\mathrm{Body}}_{\mathrm{cam}} \cdot R_{\mathrm{ref}}(\theta) \cdot \left\| \begin{bmatrix} \lambda_x & 0 & d_x \\ 0 & \lambda_y & d_y \\ 0 & 0 & -f + \Delta f \end{bmatrix} \begin{bmatrix} j_0 - j + \Delta j_0 \\ i_0 - i + \Delta i_0 \\ -1 \end{bmatrix} \right\| \quad (5)$$

where $\overrightarrow{P}^{ij}_{\mathrm{ECEF}} = (X^{ij}_{\mathrm{ECEF}}, Y^{ij}_{\mathrm{ECEF}}, Z^{ij}_{\mathrm{ECEF}})^{\mathrm{T}}$ is practical position vector of object $P$ in ECEF, and $(X^{\mathrm{sat}}_{\mathrm{ECEF}}, Y^{\mathrm{sat}}_{\mathrm{ECEF}}, Z^{\mathrm{sat}}_{\mathrm{ECEF}})^{\mathrm{T}}$ is the satellite position vector in ECEF. $\mu$ is the scale factor corresponding to the LOS vector, and the other variables have the same meanings of (1) to (4). It can be seen from (5) that the established RGPM of TIS is associated with many types of variables, and each of them could leave a special effect on the ultimate positioning accuracy, which will be analyzed elaborately in Section III-A2.

*2) Positioning Error Analysis for TIS:* In accordance with the established procedure, the error resources can be divided into interior orientation errors, exterior orientation errors, and other associated errors.

1) *Interior Orientation Errors:* Generally, interior orientation errors comprise the practical deviation from the ideal situation of principle point and distance, the ubiquitous optical and physical distortions, as well as the inevitable associated displacements during launch. As shown in Fig. 1, the interior orientation errors determine the actual pointing bias of the LOS vector exiting from the optical lens in CCS. For SDGSAT-1 TIS, dissimilarly, the 1-D scanning mirror is, however, one of the most important parts of geometric imaging links. Therefore, the assembly error and the angular measurement error of scanning mirror contribute a lot to the final positioning accuracy. Distinctively, the principle point, principle distance, and distortions depict the geometric orientation of each pixel from the focal plane to the outside of the optical lens in the camera imaging link, which decides the actual positioning accuracy of every sampling line of TIS, especially in the along-track direction, and correspondingly, the interior errors of the scanning mirrors actually portray the pointing geometry bias of every scanning line in the cross-track direction during whisk-broom imaging. Therefore, it is clear that for achieving high-precision geometric accuracy, the principle point and distance, distortions, and the assembly and angular measurements of the scanning mirror should be calibrated efficaciously.
2) *Exterior Orientation Errors:* Exterior orientation errors usually represent the installation displacements between the camera and satellite, which determines the overall deviation of the whole collected image. Actually, EOPs comprising three independent angles, however, have the ability to compensate for different kinds of overall exterior rotation errors, such as the probably existing systematic drifts of attitude and orbit errors. In terms of SDGSAT-1 TIS, according to the aforementioned analysis, the assembly error of the scanning mirror, also characterized with installation angles, has similar effects of EOPs on positioning results. Therefore, the generalized EOPs could not only modify all the overall exterior deviations but suffice to compensate for some interior errors.
3) *Other Errors:* Except for interior and exterior orientation errors analyzed above, the other error resources, such as the extraction error of GCPs, the jitter of the satellite platform, the time synchronization errors between imaging instant and the sampling moment of attitudes and orbits, as well as the atmospheric refraction error, are able to leave different degrees of influence on positioning results. And especially, atmospheric refraction error associated with incident zenith angle are not negligible for the large-angle side swing or pitch observations, which should be considered in particular for the expansion observation mode of SDGSAT-1 TIS. Besides, the launch shock, gravity release, and structural stress relief of assembled instrument could also occupy a certain proportion in the final positioning accuracy. Meanwhile, the spatial thermal deformation deriving from the change of orbital thermal environment is another factor playing a part in overall positioning accuracy [9], [21].

## B. Proposed In-Orbit GC Strategy for TIS

*1) Framework of In-Orbit GC of TIS:* Compared with space staring area-array camera and push-broom linear-array camera,

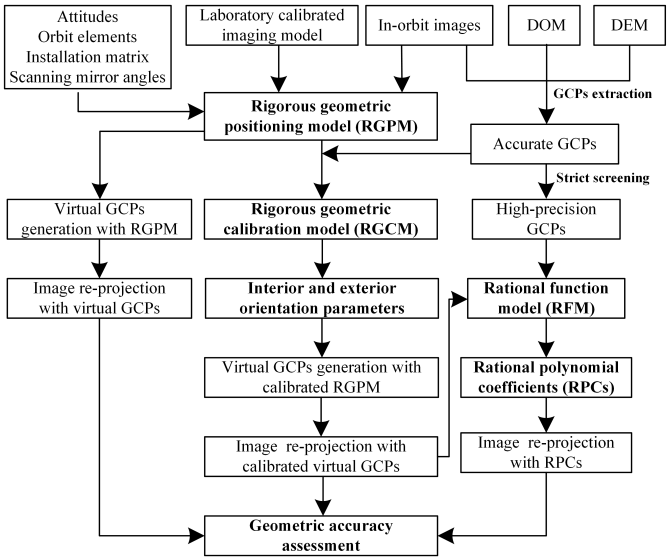


Fig. 4. Framework for in-orbit GC of SDGSAT-1 TIS.

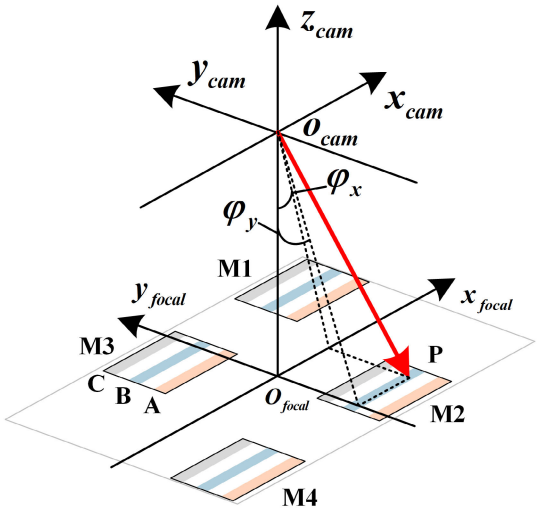


Fig. 5. Two-dimensional look-angle model of TIS.

TIS with the multimodule-spliced long-linear-array detector and wide-range whisk-broom imaging mechanism have more positioning error resources, and the complicated relationship among the different types of errors makes it more difficult to achieve a complete in-orbit GC. In this article, according to the imaging peculiarity of TIS, we proposed a novel three-step in-orbit GC strategy in which the IOPs, EOPs, and SCPs are employed to correct the positioning error of TIS.

As shown in Fig. 4, the framework for in-orbit GC of SDGSAT-1 TIS is introduced elaborately. First, based on the laboratory-calibrated parameters of the imaging model, ephemeris and attitudes, installation matrices, and the obtained in-orbit images, the RGPM is established. Second, the corresponding RGCM is constructed and calibrated with extracted accurate GCPs from the referencing DOM and DEM. Meanwhile, for eliminating the positioning errors cross-track, a fifth-degree polynomial was proposed to compensate for the angular displacement of the scanning mirror. Then, the RFM solved with high-precision GCPs is employed to correct the local nonlinear distortions of calibrated images. Finally, lots of evenly distributed GCPs are adapted to perform the geometric accuracy assessment.

*2) Construction of GC Model for TIS:* According to the error analysis in Section III-A, it should be noticed that the positioning errors defined in CCS are comprised of the errors of principle point and distance, distortions, installation angles, and the measurement angle of the scanning mirror. Especially, except for the scanning mirror angular error that affects the positioning accuracy cross-track, all the other positioning error resources could leave a nonnegligible effect on the ultimate geometric accuracy in both along-track and cross-track, and more importantly, it must be noticed that all the components of the two directions are highly correlate with each other, and the results are derived from the mutual coupling of multivariate errors, which makes it almost impossible to obtain all the corresponding IOPs accurately by decoupling.

For addressing the problems, as shown in Fig. 5, we construct a 2-D look-angle model (TLM) to characterize the interior geometry of TIS and modify the interior orientation errors, which has been successfully demonstrated and employed in in-orbit GC of many optical satellites, like ZiYuan-1 02C, ZiYuan-3, Haiyang-1C, and GaoFen-1/2/4/6 [9], [16], [17], [22], [23]. It is expressed as in (6), shown at the bottom of the page, where $(i, j)$ is the pixel coordinate of the detector in the focal plane, $(a_0, a_1, a_2, a_3, a_4, a_5, a_6, a_7, a_8)$, $(b_0, b_1, b_2, b_3, b_4, b_5, b_6, b_7, b_8)$ are the coefficients of the TLM and also taken as the interior calibration parameters, and $(\varphi_x, \varphi_y)$ means the two look-angle of pixel $(i, j)$.

In terms of the consecutive images collected during the whole scan period, TLM is, however, able to correct the positioning error along the long-linear-array detector (along-track), but cannot correct the positioning error from the scanning mirror. Moreover, practical imaging results show that the positioning error in cross-track turns out to be larger than that of along-track because of the wide-range swing and angular measurement error of the scanning mirror. Considering the rapid reciprocating motion of scanning mirror and the jitter of the satellite platform, the errors of different frequencies may also introduce uncertain positioning errors cross-track. For modifying different types of positioning errors in scanning direction, the fifth-degree polynomial is proposed to compensate for the angular displacement of the scanning mirror and

$$\overrightarrow{P_{ij}} = \begin{bmatrix} \tan\varphi_x \\ \tan\varphi_y \\ -1 \end{bmatrix} = \begin{bmatrix} a_0 + a_1 i + a_2 j + a_3 ij + a_4 i^2 + a_5 j^2 + a_6 i^2 j + a_7 ij^2 + a_8 i^3 + a_8 j^3 \\ b_0 + b_1 i + b_2 j + b_3 ij + b_4 i^2 + b_5 j^2 + b_6 i^2 j + b_7 ij^2 + b_8 i^3 + b_8 j^3 \\ -1 \end{bmatrix} \tag{6}$$

correct the positioning error cross-track as

$$\theta_k^c = c_0 + c_1\theta_k + c_2\theta_k^2 + c_3\theta_k^3 + c_4\theta_k^4 + c_5\theta_k^5 \tag{7}$$

where $\theta_k$ is the practical angular measurement result of scanning mirror of k-th sampling, $\theta_k^c$ is the corrected angle corresponding to $\theta_k$, and $(c_0, c_1, c_2, c_3, c_4, c_5)$ means the correction coefficients of the fifth-degree polynomial, namely the SCPs.

Beside the constructed interior correction models, the exterior positioning errors, including the measurement errors of attitudes, orbital elements, and installation angles, are also nonnegligible. It can be clearly seen from (3) that the transformation from $\overrightarrow{\mathrm{LOS}}_{\mathrm{cam}}^{ij}$ to $\overrightarrow{\mathrm{LOS}}_{\mathrm{ECEF}}^{ij}$ could be represented with a series of rotation matrices. In fact, the orbital element errors could introduce equivalent translation positioning errors in ECEF, and the errors of attitudes and installation angles could generate equivalent rotation positioning errors; however, the translation errors of orbit elements could be equivalently substituted as the special rotation quantities. Therefore, it is appropriate to correct the exterior positioning errors with a generalized bias correction rotation matrix as

$$\begin{bmatrix} X_{\mathrm{ECEF}} \\ Y_{\mathrm{ECEF}} \\ Z_{\mathrm{ECEF}} \end{bmatrix} = \begin{bmatrix} X_{\mathrm{ECEF}}^{\mathrm{sat}} \\ Y_{\mathrm{ECEF}}^{\mathrm{sat}} \\ Z_{\mathrm{ECEF}}^{\mathrm{sat}} \end{bmatrix} + \mu \cdot R_{\mathrm{ECI}}^{\mathrm{ECEF}}(t) \cdot R_{\mathrm{Body}}^{\mathrm{ECI}} \cdot R_{\mathrm{cam}}^{\mathrm{Body}} \cdot R_G(\varphi, \omega, \kappa) \cdot R(\theta_k^c) \cdot \begin{pmatrix} \tan\varphi_x \\ \tan\varphi_y \\ -1 \end{pmatrix} \tag{8}$$

where $R_G(\varphi, \omega, \kappa)$ is the defined generalized bias correction matrix, namely the exterior calibration parameters of TIS. $\varphi, \omega$ and $\kappa$ are the corresponding generalized bias correction angles of $R_G$. The other variables have the same meanings as (5). Equation (8) is the rigorous GC model (RGCM) of TIS. Generally, the exterior calibration parameters of RGCM are adopted to correct the overall geo-location displacements of the collected images, and the interior calibration parameters are responsible for eliminating relative geometric errors in the image.

*3) Estimation of the Calibration Parameters:* In this article, the three-step in-orbit GC method is adopted to estimate the calibration parameters of TIS. Distinctly, SCPs are sequentially calculated with the least squares method during the estimation of IOPs for correcting the positioning error cross-track.

*a) Estimation of EOPs and IOPs:* From the constructed RGCM, the rigorous geometric imaging model depicting the relationship from the object in ECEF to the corresponding image point in PCS can be expressed as

$$\begin{pmatrix} \tan\varphi_x \\ \tan\varphi_y \\ -1 \end{pmatrix} = \mu^{-1} \cdot R_G(\varphi, \omega, \kappa)^{-1} \cdot R_{\mathrm{ref}}(\theta_k^c) \cdot R_{\mathrm{Body}}^{\mathrm{cam}} \cdot R_{\mathrm{ECI}}^{\mathrm{Body}} \cdot R_{\mathrm{ECEF}}^{\mathrm{ECI}}(t) \cdot \begin{bmatrix} X - X^{\mathrm{sat}} \\ Y - Y^{\mathrm{sat}} \\ Z - Z^{\mathrm{sat}} \end{bmatrix}_{\mathrm{ECEF}} \tag{9}$$

where $R_G(\varphi, \omega, \kappa)^{-1}$, $R_{\mathrm{Body}}^{\mathrm{cam}}$, $R_{\mathrm{ECI}}^{\mathrm{Body}}$ and $R_{\mathrm{ECEF}}^{\mathrm{ECI}}$ are the inverse matrices of $R_G(\varphi, \omega, \kappa)$, $R_{\mathrm{cam}}^{\mathrm{Body}}$, $R_{\mathrm{Body}}^{\mathrm{ECI}}$ and $R_{\mathrm{ECI}}^{\mathrm{ECEF}}$, respectively. $(X, Y, Z)$ and $(X^{\mathrm{sat}}, Y^{\mathrm{sat}}, Z^{\mathrm{sat}})$ are the object and satellite position coordinates in ECEF.

Then based on (9), we could have the error equations as

$$\begin{cases} G_x(X_E, X_I) = \dfrac{r_{11}\overline{X} + r_{12}\overline{Y} + r_{13}\overline{Z}}{r_{31}\overline{X} + r_{32}\overline{Y} + r_{33}\overline{Z}} - \tan\varphi_x \\ G_y(X_E, X_I) = \dfrac{r_{21}\overline{X} + r_{22}\overline{Y} + r_{23}\overline{Z}}{r_{31}\overline{X} + r_{32}\overline{Y} + r_{33}\overline{Z}} - \tan\varphi_y \end{cases} \tag{10}$$

in which $G_x$ and $G_y$ are the residual errors in along-track and cross-track, respectively, and $X_E$ and $X_I$ are the EOPs and IOPs to be calibrated, respectively

$$\begin{cases} \begin{pmatrix} \overline{X} \\ \overline{Y} \\ \overline{Z} \end{pmatrix} = R_{\mathrm{ref}}(\theta_k^c) \cdot R_{\mathrm{Body}}^{\mathrm{cam}} \cdot R_{\mathrm{ECI}}^{\mathrm{Body}} \cdot R_{\mathrm{ECEF}}^{\mathrm{ECI}}(t) \cdot \begin{bmatrix} X - X^{\mathrm{sat}} \\ Y - Y^{\mathrm{sat}} \\ Z - Z^{\mathrm{sat}} \end{bmatrix}_{\mathrm{ECEF}} \\ R_G(\varphi, \omega, \kappa)^{-1} = \begin{bmatrix} r_{11} & r_{12} & r_{13} \\ r_{21} & r_{22} & r_{23} \\ r_{31} & r_{32} & r_{33} \end{bmatrix}. \end{cases} \tag{11}$$

For estimating the EOPs of TIS, we should first obtain the initial values of IOPs with laboratory-calibrated results and the practical measurement scanning mirror angles, and meanwhile, we take the calibrated installation angles between CCS and SBCS in the laboratory for the initial values of EOPs. Assuming the IOPs and the scanning mirror measurements are the true values, the error equations of $i$th GCPs could be expressed with the increment of EOPs as

$$V_i = A_i \Delta X_E - L_i P_i \tag{12}$$

where $A_i$ is the coefficient matrix consisting of the partial derivatives referencing to the elements of EOPs, $\Delta X_E$ is the increment of EOPs, $L_i$ is the residual vector, and $P_i$ is the weight factor of $i$th GCPs. According to the iterative least squares method, the increment of EOPs could be estimated as

$$\Delta X_E = (A^T P A)^{-1}(A^T P L). \tag{13}$$

Then we could have the updated EOPs as

$$X_E^{m+1} = X_E^m + \Delta X_E \tag{14}$$

where $X_E^{m+1}$ and $X_E^m$ are the updated EOPs of the $(m+1)$th and $m$th iterations, $\Delta X_E$ is the corresponding increment of EOPs. Then repeat the estimation steps until the change of increment meets the limited demand.

Similarly, after the estimation of EOPs, we assume obtained EOPs as the true values; the error equations of $i$th GCPs could be expressed with the increment of IOPs as

$$V_i = B_i \Delta X_I - L_i P_i \tag{15}$$

where $B_i$ is the coefficient matrix consisting of the partial derivatives referencing the elements of IOPs, and $\Delta X_I$ is the increment of IOPs. Similarly, the increment of IOPs could be estimated as

$$\Delta X_I = (B^T P B)^{-1}(B^T P L). \tag{16}$$

The updated IOPs could be expressed as

$$X_I^{m+1} = X_I^m + \Delta X_I \tag{17}$$

where $X_I^{m+1}$ and $X_I^m$ are the updated IOPs of the $(m+1)$th and $m$th iterations, $\Delta X_I$ is the corresponding increment of IOPs. Similarly, repeat the estimation steps until the change of the increment meets the limited demand.

*b) Estimation of SCPs:* It should be noticed the constructed RGCM actually describes the mapping relationship of a special imaging instant from the image point in FPCS to the object in ECEF. The estimation of the EOPs and IOPs above could effectively correct the overall exterior geo-location displacements and the interior geometric errors mainly along-track but cannot remove the pointing error deriving from the scanning mirror cross-track. In order to eliminate the positioning error cross-track, we propose a least-square-based calculating method along with the iterative convergence algorithm of Levenberg-Marquardt (LM) to estimate the SCPs of the scanning mirror. According to the calibrated RGCM of TIS, we could have

$$\overrightarrow{\mathrm{LOS}}_G^n = R_{\mathrm{ref}}(\theta_k) \cdot \overrightarrow{\mathrm{los}}_{\mathrm{cam}}^{ij} \tag{18}$$

$$\begin{cases} \overrightarrow{\mathrm{LOS}}_G^n = R_{\mathrm{ECEF}}^G \cdot \left\| X_n - X^{\mathrm{sat}}, Y_n - Y^{\mathrm{sat}}, Z_n - Z^{\mathrm{sat}} \right\|^T \\ R_{\mathrm{ECEF}}^G = R_G(\varphi, \omega, \kappa)^{-1} \cdot R_{\mathrm{Body}}^{\mathrm{cam}} \cdot R_{\mathrm{ECI}}^{\mathrm{Body}} \cdot R_{\mathrm{ECEF}}^{\mathrm{ECI}} \\ \overrightarrow{\mathrm{los}}_{\mathrm{cam}}^{ij} = \left\| \tan\varphi_x, \tan\varphi_y, -1 \right\|^T \end{cases} \tag{19}$$

in which $\overrightarrow{\mathrm{LOS}}_G^n$ is the unit vector from satellite to $n$th GCPs in CCS. $\overrightarrow{\mathrm{los}}_{\mathrm{cam}}^{ij}$ is the unit exit vector of pixel $(i, j)$ corresponding to the $n$th GCPs. $R_{\mathrm{ref}}(\theta_k)$ is the reflect matrix of scanning mirror, and $\theta_k$ is the corrected position angle corresponding to practical measurements of $\theta$. For a exact GCPs, the associated $\overrightarrow{\mathrm{LOS}}_G^n$, $\overrightarrow{\mathrm{los}}_{\mathrm{cam}}^{ij}$ and $\theta$ are known, then (18) could be expressed as a function of SCPs as

$$\overrightarrow{\mathrm{LOS}}_G^n = \theta_k^c(c_0, c_1, c_2, c_3, c_4, c_5) \cdot \overrightarrow{\mathrm{los}}_{\mathrm{cam}}^{ij} \tag{20}$$

where $\theta_k^c = \sum_{i=0}^5 c_i \theta^i$ is the fifth-degree scanning compensation polynomial. Based on the least square method and LM algorithm, the SCPs can be calculated with the GCPs as

$$\min_{c_0,c_1,c_2,c_3,c_4,c_5} \sum_{n=1}^{N} \left\langle \overrightarrow{\mathrm{LOS}}_G^n, R_{\mathrm{ref}}\left(\theta_k^c(c_0, c_1, c_2, c_3, c_4, c_5)\right) \cdot \overrightarrow{\mathrm{los}}_{\mathrm{cam}}^{ij} \right\rangle^2 \tag{21}$$

where $N$ is the number of GCPs. $\langle \vec{A}, \vec{B} \rangle$ means the intersection angle of vector $\vec{A}$ and $\vec{B}$.

It can be seen that the proposed three-step in-orbit GC strategy of TIS have many advantages. First, the geometric errors of different kinds and properties could be eliminated efficiently because the EOPs, IOPs and SCPs have the ability to compensate for the linear errors (rotation, translation, scaling), nonlinear errors (optical distortions), even the different frequency errors (scanning motion, platform jitter). Second, the division of positioning errors like exterior and interior, along-track, and cross-track makes it possible and convenient to analyze the effects of different factors individually. Finally, this method provides a new idea for accurately calibrating the space-based optical payloads with a complicated imaging mechanism, especially for the super-wide-range whisk-broom optical cameras.

TABLE II
CHARACTERISTICS OF THE EXPERIMENTAL DATA

| Scenes | Acquisition time | Imaging area | Terrain type |
|---|---|---|---|
| **Scene 1** | 2022.07.07 21:44:06 | E114.7 N32.1 | Mountains, plains |
| **Scene 2** | 2022.09.01 09:55:07 | E121.71 N40.8 | Plains |
| **Scene 3** | 2022.10.24 09:22:35 | E131.69 N47.64 | Hills, plains |

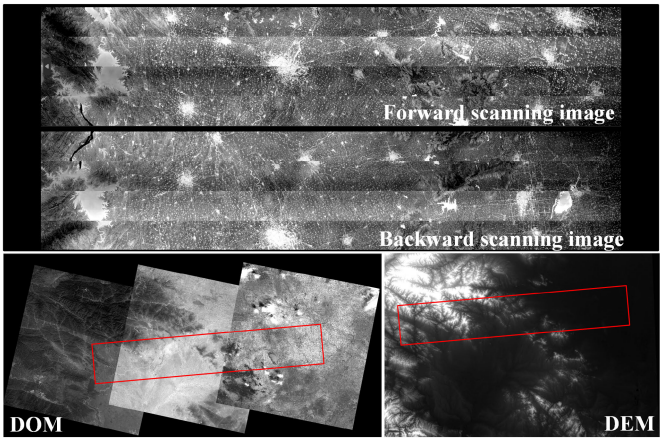


Fig. 6. Experimental data of in-orbit forward and backward scanning images, reference DOM and DEM.

### C. Positioning Accuracy Assessment

To effectively evaluate the positioning quality of SDGSAT-1 TIS images, plenty of even-distributed GCPs extracted from the calibrated images and corresponding reference images are adopted to calculate the absolute positioning accuracy, namely the average error and the root-mean-squared error (RMSE) of three bands in along-track, cross-track, as well as the plane, respectively. The RMSE is determined as follows:

$$\mathrm{RMSE} = \sqrt{\frac{\sum_{i=1}^{N} \left( e_{i,\text{along-track}}^2 + e_{i,\text{aross-track}}^2 \right)}{N}} \tag{22}$$

where $N$ is the total number of the extracted GCPs, $e_{i,\text{along-track}}$ and $e_{i,\text{cross-track}}$ are the geo-location coordinates residuals of the $i$th GCPs from calibrated images and corresponding reference images, respectively.

## IV. EXPERIMENTAL RESULTS AND DISCUSSION

### A. Experimental Data

In this section, for verifying the proposed method, three obtained cloud-free scenes distinguished with the cloud detection method [35], including the forward and backward scanning images collected on 2022-07-07, 2022-09-01, and 2022-10-24, covering various terrains of hills, plains, and mountains, are selected to perform in-orbit GC for practical geometric assessment. Table II shows the detailed characteristics of experimental data. Meanwhile, in consideration of the 30 m resolution TIRIs of SDGSAT-1 TIS, the panchromatic images of Landsat 8 with a 12 m circular error at a 90% confidence level are adopted as a planar reference, namely the DOM. And as shown in Fig. 6, because of the 300 km wide swath of TIS, we have to splice two or three associated panchromatic images of Landsat 8 to achieve an

entire coverage of the calibration regions. In addition, the 30 m version 2 of advanced spaceborne thermal emission and reflection radiometer (ASTER) global digital elevation model (GDEM) is used as a DEM reference for acquiring elevation information. As shown in Fig. 6, the red blocks approximately show the corresponding DOM and DEM ranges of in-orbit TIS images.

It should be noticed that large nonlinear radiation differences, inconsistent resolution, and the large geometric distortions between in-orbit TIS TIRIs and Landsat 8 panchromatic images make it extremely difficult to obtain enough adequate and accurate calibrating and checking GCPs. In this article, aiming to guarantee the number and accuracy of GCPs, we first adopt the Morevac and cross-correlation algorithms to search and find the local image blocks with remarkable features [1]. Then, the RIFT [19] is employed to extract corresponding GCPs in every image pair. And for achieving high-precision registrations among three bands, the GCPs of bands A and C are determined based on the GCPs of band B. Especially the image blocks around obtained GCPs of Landsat 8 panchromatic images and cross-correlation algorithm are used to extract corresponding GCPs from bands A and B images of SDGSAT-1 TIS. In order to explore the variation tendency of the positioning errors in along-track and cross-track directions and reveal the effects of scanning mirrors on geometric accuracy, GCPs evenly distributed in sample and line directions are required.

### *B. Experimental Results and Discussion*

As shown in Fig. 1, since the three bands' long-linear-array detectors, arranged in the same focal plane in parallel, have a common optical path, we selected the forward and backward scanning images of band B as an example to introduce the calibration results. The associated results of other bands of different scenes are counted and listed in the tables below. First, in accordance with the GCPs extraction methods, 896 GCPs, and 834 GCPs have been obtained from the forward and backward scanning images of scene 1 band B. Considering some of the GCPs are concentrated in specific areas, the grid-based nonmaximum suppression was used to guarantee the even distribution in the entire image. After abandoning the redundant GCPs, 581 GCPs and 557 GCPs evenly distributed in the forward and backward scanning images of scene 1 band B are eventually screened out. Then the GCPs datasets are divided into two parts equally. One is adopted to estimate the calibration parameters of the TIS, and the other is employed to evaluate the effectiveness of the results.

*1) Direct Positioning Results:* Based on the established RGPM of SDGSAT-1 TIS, we first calculate the direct absolute positioning errors in along-track and cross-track directions of forward and backward scanning images with GCPs. As the scatter shown in Fig. 7, the blue upward triangle and downward red triangle show the calculated direct positioning errors in along-track and cross-track of the forward and backward scanning images, respectively. It can be clearly observed that positioning errors in cross-track is larger than that of along-track, which means the total installation angular displacement

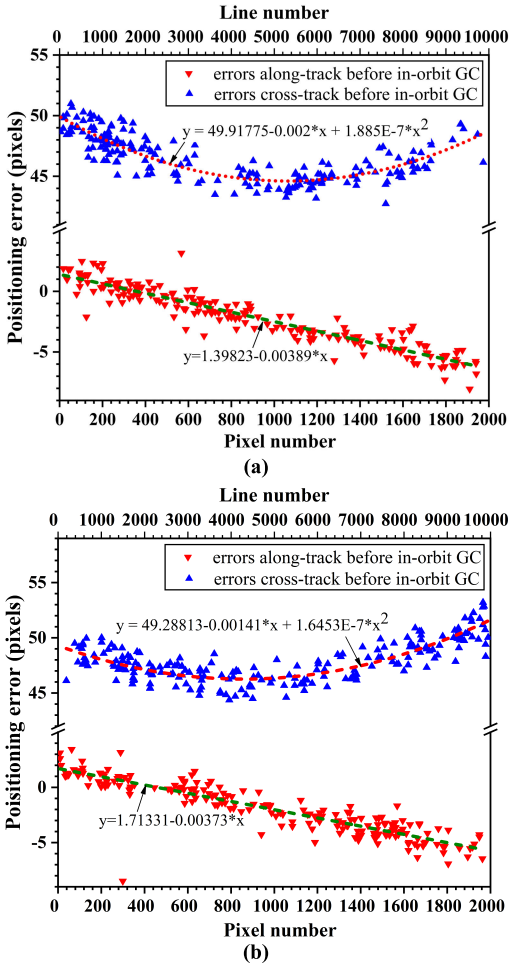


Fig. 7. Positioning errors in along-track and cross-track of Band B (a) forward scanning images and (b) backward scanning images before in-orbit GC of Scene 1.

in roll direction is worse than that in pitch direction after launch. And for one thing, the positioning errors in cross-track present a distinct systematic tendency. Especially, it becomes larger with the increasement of distance from the middle scanning line of whisk-broom image and can be precisely fit with a quadratic polynomial, which indicates the symmetry in cross-track. According to the RGPM of TIS, the control error and angular measurement error of the scanning mirror is known to have an important impact on the LOS pointing accuracy. And with the growth of scanning angle, the ground positioning errors deriving from the same magnitude errors of the scanning mirror ought to be different. Therefore, considering the coincidence between the cross-track direction and the scanning direction of the scanning mirror, it is totally certain that the errors from the scanning mirror could leave a systematic effect on the ground positioning errors in the cross-track. For another, the positioning errors in the along-track direction show great linearity, and there is an obvious displacement from the zero-axis. Meanwhile, in order to present the total positioning results, the planar positioning error vectors of forward and backward scanning images are calculated and exhibited in Fig. 8(a) and (b). It could be found obviously that before in-orbit GC, there is an overall displacement in the geo-location coordinates of the images.

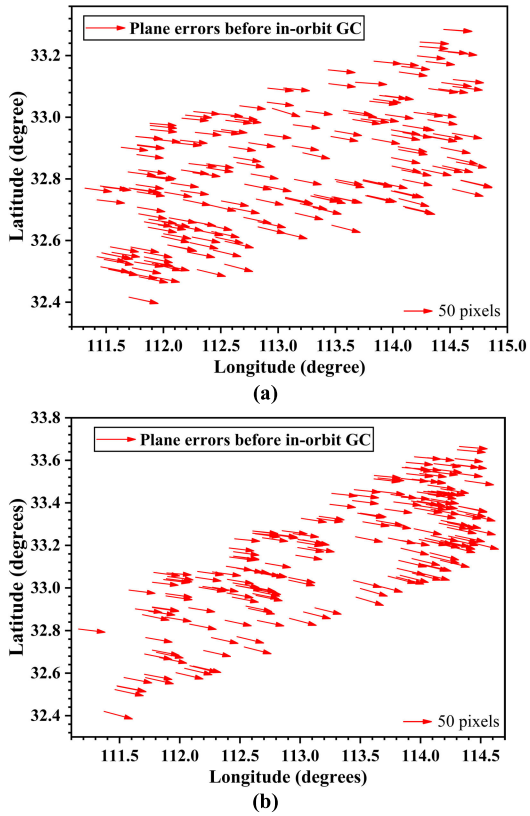


Fig. 8. Plane errors in along-track and cross-track of Band B (a) forward scanning images and (b) backward scanning images before in-orbit GC of Scene 1.

TABLE III
EOPs BEFORE AND AFTER IN-ORBIT GC (UNIT: DEGREE)

| Band | EOPs | Forward scanning image | | Backward scanning image | |
|---|---|---|---|---|---|
| | | Before GC | After GC | Before GC | After GC |
| A | φ | 0.0 | 0.3861 | 0.0 | 0.3973 |
| | ω | 0.0 | 0.1127 | 0.0 | 0.1092 |
| | κ | 0.0 | -0.0137 | 0.0 | -0.0054 |
| B | φ | 0.0 | 0.4001 | 0.0 | 0.3877 |
| | ω | 0.0 | 0.2033 | 0.0 | 0.1572 |
| | κ | 0.0 | -0.0003 | 0.0 | 0.0001 |
| C | φ | 0.0 | 0.3911 | 0.0 | 0.4096 |
| | ω | 0.0 | 0.1127 | 0.0 | 0.1127 |
| | κ | 0.0 | 0.0001 | 0.0 | -0.0018 |

In accordance with Figs. 7 and 8, it is not difficult to conclude that overall displacements and systematic and trended errors exist in the final positioning errors of forward and backward scanning images of TIS. And based on the analysis of Section III, it can be deduced that the overall displacements of the images have something to do with the deviation of the exterior parameters, namely the installation angles of TIS, which could be calibrated effectively with EOPs. And the systematic and trended errors in along-track and cross-track have special but certain relationships with the camera parameters, including the angular measurement of the scanning mirror, distortions, principle point, and distance, and can be corrected with the IOPs and SCPs.

*2) Positioning Results After in-Orbit GC:* Based on the proposed calibration method, the GC parameters of TIS are estimated successfully with acquired GCPs. And for verifying the commonality of exterior calibration parameters, we calculate the EOPs of three bands of forward and backward scanning images of TIS. Table III shows the EOPs before and after in-orbit GC. Especially it should be noticed that the EOPs after in-orbit GC mean the increments of three installation angles corresponding to the initial value calibrated before launch. According to the frame coordinate systems defined in Section III, the installation angular errors in pitch and roll directions will affect the positioning errors in along-track and cross-track, respectively. The yaw errors can influence the positioning errors both in along-track and cross-track directions. It can be seen from Table III that calibrated angle in the roll direction is much larger than those in the pitch and yaw directions because the positioning errors in the cross-track, corresponding to roll angle, are approximately far greater than that in the along-track. Additionally, the EOPs magnitude of the three bands of forward and backward scanning images are almost constant, which demonstrates the commonality of the estimated TIS EOPs. The value fluctuation of EOPs may be related to GCPs extraction accuracy and other noises.

Meanwhile, the positioning error after in-orbit GC of the experimental scenes, collected in the same orbit but not the particular calibration scenes, are calculated by checking GCPs. And similarly, the scatters of positioning errors in the along-track and cross-track of band B forward and backward scanning images are drew in Fig. 9, respectively. It can be observed that after in-orbit GC, the position errors both in along-track and cross-track are greatly decreased. The majority of positioning errors are within $\pm 1.5$ pixels. And more importantly, the systematic and trended errors are also modified, which effectively demonstrates the effectiveness of the proposed in-orbit GC strategy. In addition, for evaluating the overall positioning accuracy after in-orbit GC, the planar positioning error vectors of the same forward and backward scanning images are also plotted and displayed in Fig. 10(a) and (b). It can be seen distinctly that, except for a few anomalies, the planar error vectors of the involved images after in-orbit GC all degrade to a small enough magnitude. And furthermore, the systematic orientations of the error vectors in Fig. 7(a) and (b) disappear absolutely, which, on the other hand, reflects the soundness and validity of the proposed method as well.

Focusing on revealing and comparing the calibrated results quantitatively, we count the mean and the RMSE of positioning errors of forward and backward scanning images of different bands and different scenes before and after in-orbit GC elaborately and list them together in Table IV. Meanwhile, in order to explore the calibration differences among the three bands, the mean and RMSE of positioning errors in along-track, cross-track, and the plane of the same band of three scenes are calculated and exhibited in Table V. Similarly, for researching the geometric accuracy of different scanning images, as shown in Table IV, we calculate and analyze the positioning results of forward and backward scanning images before and after in-orbit GC. And the mean and RMSE of the positioning errors in along-track, cross-track, and the plane of different images before and after in-orbit GC are also counted

TABLE IV
POSITIONING RESULTS OF THREE SCENES BEFORE AND AFTER IN-ORBIT GC (UNIT: PIXELS)

| Images | Band | GCPs | Methods | Forward scanning images (Mean/RMSE) | | | Backward scanning images (Mean/RMSE) | | |
|---|---|---|---|---|---|---|---|---|---|
| | | | | Along-track | Cross-track | Plane | Along-track | Cross-track | Plane |
| Scene1 | A | 254 | Before GC | 2.58/1.93 | 46.59/1.91 | **46.66/2.72** | 2.42/1.68 | 47.88/1.86 | **47.94/2.50** |
| | | | After GC | 0.49/0.57 | 0.70/0.64 | **0.85/0.85** | 0.58/0.74 | 1.13/1.05 | **1.27/1.28** |
| | B | 243 | Before GC | 2.51/1.91 | 46.53/1.89 | **46.59/2.68** | 2.51/1.76 | 47.85/1.84 | **47.91/2.55** |
| | | | After GC | 0.47/0.54 | 0.68/0.60 | **0.83/0.84** | 0.52/0.71 | 0.85/0.80 | **0.99/1.08** |
| | C | 249 | Before GC | 2.43/1.86 | 46.48/1.88 | **47.81/2.59** | 2.63/1.84 | 47.74/1.83 | **47.81/2.59** |
| | | | After GC | 0.48/0.54 | 0.69/0.58 | **0.84/0.79** | 0.63/0.70 | 1.19/1.05 | **1.34/1.26** |
| Scene2 | A | 206 | Before GC | 2.71/1.73 | 46.87/1.99 | **46.95/2.63** | 2.58/1.69 | 47.79/1.86 | **47.86/2.51** |
| | | | After GC | 0.51/0.58 | 0.74/0.69 | **0.89/0.9** | 0.59/0.77 | 0.93/0.85 | **1.10/1.15** |
| | B | 219 | Before GC | 2.67/1.89 | 46.79/1.91 | **46.86/2.68** | 2.49/1.73 | 47.78/1.84 | **47.84/2.53** |
| | | | After GC | 0.48/0.52 | 0.71/0.68 | **0.85/0.85** | 0.58/0.73 | 0.91/0.79 | **1.08/1.08** |
| | C | 236 | Before GC | 2.69/1.92 | 46.81/1.95 | **46.88/2.73** | 2.57/1.81 | 47.83/1.83 | **47.90/2.57** |
| | | | After GC | 0.53/0.55 | 0.73/0.63 | **0.90/0.83** | 0.61/0.75 | 0.94/0.82 | **1.12/1.11** |
| Scene3 | A | 203 | Before GC | 2.59/1.97 | 46.69/1.97 | **46.76/2.78** | 2.61/1.71 | 47.93/1.91 | **48.00/2.56** |
| | | | After GC | 0.52/0.53 | 0.71/0.69 | **0.88/0.87** | 0.65/0.75 | 0.91/0.85 | **1.12/1.13** |
| | B | 206 | Before GC | 2.61/1.92 | 46.71/1.92 | **46.78/2.71** | 2.59/1.69 | 47.89/1.89 | **47.96/2.54** |
| | | | After GC | 0.48/0.49 | 0.69/0.71 | **0.84/0.86** | 0.62/0.75 | 0.89/0.82 | **1.08/1.11** |
| | C | 211 | Before GC | 2.63/1.89 | 46.78/1.98 | **46.85/2.73** | 2.64/1.73 | 47.90/1.93 | **47.97/2.59** |
| | | | After GC | 0.55/0.59 | 0.75/0.70 | **0.93/0.91** | 0.67/0.75 | 0.95/0.84 | **1.16/1.13** |

TABLE V
POSITIONING RESULTS OF DIFFERENT BANDS BEFORE AND AFTER IN-ORBIT GC (UNIT: PIXELS)

| Band | Method | Mean | | | RMSE | | |
|---|---|---|---|---|---|---|---|
| | | Along-track | Cross-track | Plane | Along-track | Cross-track | Plane |
| A | Before GC | 2.58 | 47.29 | 47.36 | 1.79 | 1.92 | 2.62 |
| | After GC | **0.56** | **0.85** | **1.02** | **0.66** | **0.80** | **1.03** |
| B | Before GC | 2.56 | 47.26 | 47.33 | 1.82 | 1.88 | 2.62 |
| | After GC | **0.53** | **0.79** | **0.95** | **0.62** | **0.73** | **0.96** |
| C | Before GC | 2.60 | 47.26 | 47.33 | 1.84 | 1.90 | 2.65 |
| | After GC | **0.58** | **0.88** | **1.05** | **0.65** | **0.77** | **1.01** |

TABLE VI
POSITIONING RESULTS OF DIFFERENT SCANNING IMAGES BEFORE AND AFTER IN-ORBIT GC (UNIT: PIXELS)

| Items | Method | Mean | | | RMSE | | |
|---|---|---|---|---|---|---|---|
| | | Along-track | Cross-track | Plane | Along-track | Cross-track | Plane |
| Forward scanning images | Before GC | 2.60 | 46.69 | 46.77 | 1.89 | 1.93 | 2.71 |
| | After GC | **0.50** | **0.71** | **0.87** | **0.55** | **0.66** | **0.86** |
| Backward scanning images | Before GC | 2.56 | 47.84 | 47.91 | 1.74 | 1.87 | 2.55 |
| | After GC | **0.61** | **0.97** | **1.14** | **0.74** | **0.87** | **1.15** |

and displayed in Table VII to figure out the overall positioning accuracy in different directions.

It is evident from Table IV that before in-orbit GC, the means of positioning errors of all forward and backward scanning images in along-track and cross-track directions are more than 2.4 and 46.4 pixels, respectively. And meanwhile, there is a fluctuation of around 2.0 pixels (RMSE) in the both directions. In contrast, after in-orbit GC, the corresponding means of positioning errors turn out to be less than 0.6 and 0.8 pixels in along-track and cross-track directions, respectively. And the associated RMSEs also decrease to less than 0.7 and 0.9 pixels.

As shown in Fig. 2, in the focal plane of TIS, the positions of the four detector modules of band B interleaving staggered are centrosymmetric about the original point of the FPCS; however, in the predefined coordinate system, the locations of the four detector modules of bands A and B, deviating a little from the defined origin, are not centrosymmetric about the original point but about the points in the $x$-axis, which could more or less affect the representation accuracy of the detector LOS. It can be surveyed from Table V that before in-orbit GC, the positioning errors of three bands in along-track, cross-track, and plane are almost equal to each other. Whereas after in-orbit GC, the mean and RMSE of positioning errors of band B turn out to be less than those of bands A and C. This difference, considering the consistent exterior calibration parameters, probably has something to do with the interior calibration parameters. More importantly, it should be noted that the positioning errors of all three bands, however, improve a lot after in-orbit GC.

Similarly, Table VI shows the positioning accuracy of forward and backward scanning images before and after in-orbit GC. It can be clearly observed that after in-orbit GC, the positioning errors of forward and backward scanning images

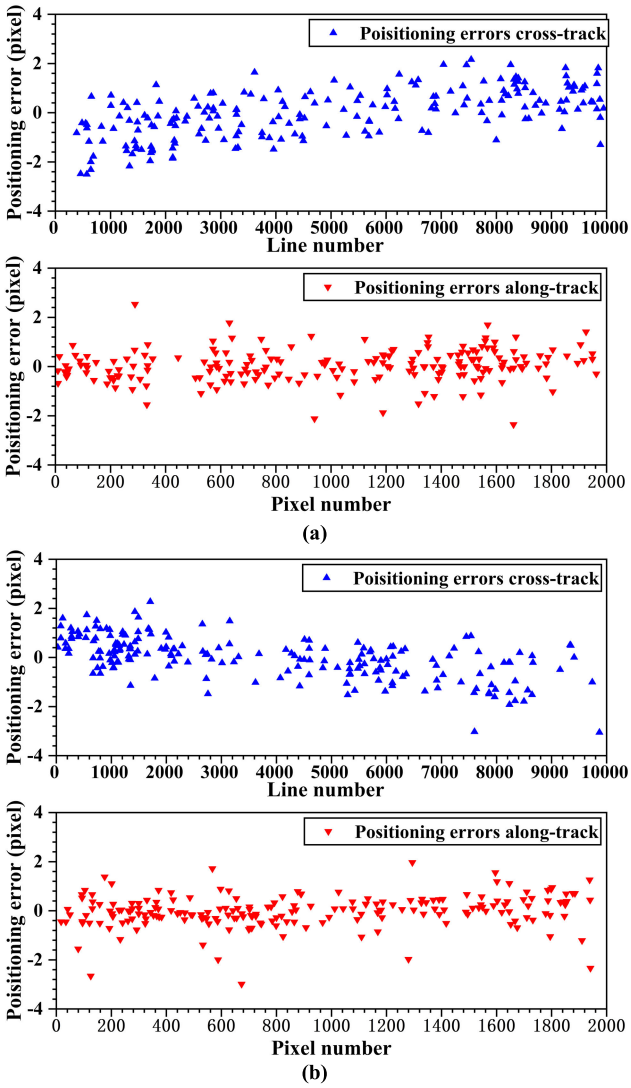


Fig. 9. Positioning errors in along-track and cross-track of Band B (a) forward scanning image and (b) backward scanning image after in-orbit GC of Scene 1.

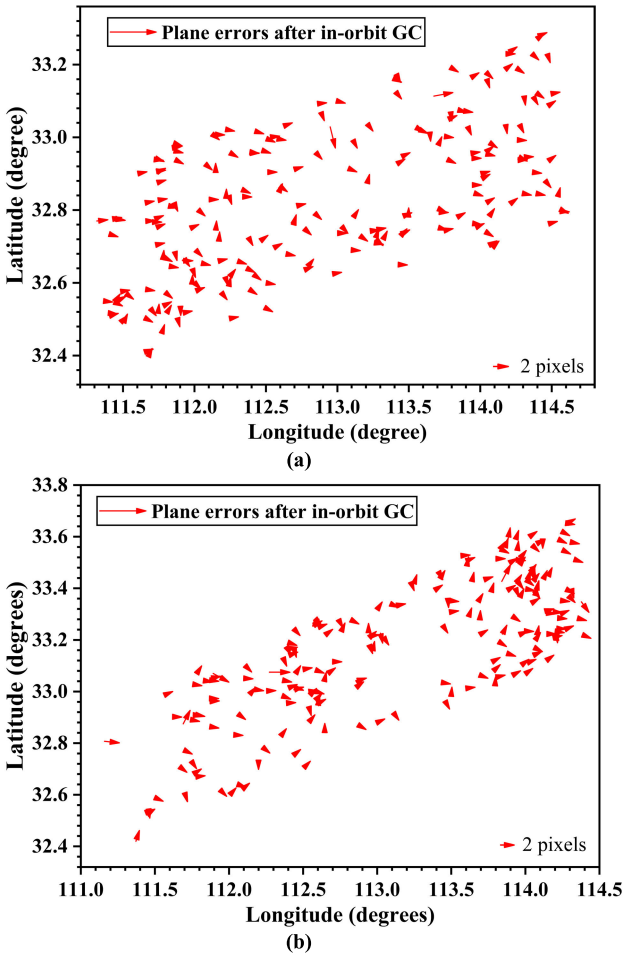


Fig. 10. Plane errors in along-track and cross-track of Band B (a) forward scanning image and (b) backward scanning image after in-orbit GC of Scene 1.

TABLE VII

POSITIONING RESULTS OF DIFFERENT DIRECTIONS BEFORE AND AFTER IN-ORBIT GC (UNIT: PIXELS)

| Items | Mean | | RMSE | |
|---|---|---|---|---|
| | Before GC | After GC | Before GC | After GC |
| Along-track | 2.58 | **0.55** | 1.81 | **0.64** |
| Cross-track | 47.27 | **0.84** | 1.90 | **0.77** |
| Plane | 47.34 | **1.03** | 2.63 | **1.01** |

are all decreased to approximately 1.0 pixels, which indicates the soundness of the proposed method for different scanning images. And more significantly, the positioning errors of forward scanning images both before and after in-orbit GC seem to be a little less than that of the backward scanning images. Meanwhile, it can be seen from Table VII that although the positioning errors in along-track, cross-track, and plane are effectively corrected after in-orbit GC, the positioning errors in cross-track are still larger than that of along-track, which may be related to angular measurement errors of the scanning mirror.

## V. CONCLUSION

The combination of a long linear-array detector and wide-range whisk-broom is an innovative and efficient way for low-orbit satellites to achieve the imaging goals of wide-swath and high-resolution simultaneously. In this article, we proposed a three-step in-orbit GC strategy, including the estimations of EOPs, IOPs, and SCPs to correct the geo-positioning errors of whisk-broom TIS aboard SDGSAT-1. The works and contributions of this article have been concluded briefly as follows: 1) the RGPM of whisk-broom TIS of SDGSAT-1 is established, and the associated positioning error resources comprising interior and exterior orientation errors and the other errors are qualitatively analyzed; 2) we also constructed the RGCM of TIS based on the TLM and generalized bias correction matrix and put forward to adopt the fifth-degree polynomial to modify the systematic errors of scanning mirror in the cross-track direction, and meanwhile, we presented a three-step estimation method to estimate the calibration parameters with GCPs; and 3) the direct positioning error

before in-orbit GC presents a tendency of small in the middle and large on both sides, and the overall deviation exceeds 47 pixels cross-track. After in-orbit GC, the positioning errors of three bands are within 1.0 pixels both in along-track and cross-track.

It could be deduced credibly that although this in-orbit GC method is proposed for whisk-broom TIS of SDGSAT-1, it is really versatile and suitable for the other space-based optical whisk-broom payloads on account of the universality of imaging mechanisms.

## REFERENCES


[1] X. Li, Z. Hu, L. Jiang, L. Yang, and F. Chen, "GCPs extraction with geometric texture pattern for thermal infrared remote sensing images," *IEEE Geosci. Remote Sens. Lett.*, vol. 19, pp. 1–5, 2022, doi: 10.1109/LGRS.2020.3030303.

[2] S. Chen, H. Ren, X. Ye, J. Dong, and Y. Zheng, "Geometry and adjacency effects in urban land surface temperature retrieval from high-spatial-resolution thermal infrared images," *Remote Sens. Environ.*, vol. 262, Sep. 2021, Art. no. 112518, doi: 10.1016/j.rse.2021.112518.

[3] D. M. Tratt, K. N. Buckland, E. R. Keim, and J. L. Hall, "Identification and source attribution of halocarbon emitters with longwave-infrared spectral imaging," *Remote Sens. Environ.*, vol. 258, Jun. 2021, Art. no. 112398, doi: 10.1016/j.rse.2021.112398.

[4] K. A. Barta, M. Hais, and M. Heurich, "Characterizing forest disturbance and recovery with thermal trajectories derived from Landsat time series data," *Remote Sens. Environ.*, vol. 282, Dec. 2022, Art. no. 113274, doi: 10.1016/j.rse.2022.113274.

[5] L. Li, L. Jiang, J. Zhang, S. Wang, and F. Chen, "A complete YOLO-based ship detection method for thermal infrared remote sensing images under complex backgrounds," *Remote Sens.*, vol. 14, no. 7, p. 1534, Mar. 2022, doi: 10.3390/rs14071534.

[6] J. Storey, M. Choate, and D. Moe, "Landsat 8 thermal infrared sensor geometric characterization and calibration," *Remote Sens.*, vol. 6, no. 11, pp. 11153–11181, Nov. 2014, doi: 10.3390/rs61111153.

[7] A. Pearlman, B. Efremova, M. Montanaro, A. Lunsford, D. Reuter, and J. McCorkel, "Landsat 9 thermal infrared sensor 2 on-orbit calibration and initial performance," *IEEE Trans. Geosci. Remote Sens.*, vol. 60, 2022, Art. no. 1002608, doi: 10.1109/TGRS.2022.3183551.

[8] H. Wang, "GF-5 VIMI on-orbit calibration instrument and performance," *J. Comput. Commun.*, vol. 7, no. 7, pp. 293–300, 2019, doi: 10.4236/jcc.2019.77024.

[9] M. Wang, Y. Cheng, X. Chang, S. Jin, and Y. Zhu, "On-orbit geometric calibration and geometric quality assessment for the high-resolution geostationary optical satellite GaoFen4," *ISPRS J. Photogramm. Remote Sens.*, vol. 125, pp. 63–77, Mar. 2017, doi: 10.1016/j.isprsjprs.2017.01.004.

[10] L. Jiang, L. Li, X. Li, J. Jiao, and F. Chen, "Extrapolating distortion correction with local measurements for space-based multi-module splicing large-format infrared cameras," *Opt. Exp.*, vol. 30, pp. 38043–38059, Oct. 2022, doi: 10.1364/OE.470476.

[11] X. Li, X. Su, Z. Hu, L. Yang, L. Zhang, and F. Chen, "Improved distortion correction method and applications for large aperture infrared tracking cameras," *Infr. Phys. Technol.*, vol. 98, pp. 82–88, May 2019, doi: 10.1016/j.infrared.2019.02.009.

[12] W. Feng, H. Wang, J. Fan, B. Xie, and X. Wang, "Geometric parameters calibration of focused light field camera based on edge spread information fitting," *Photonics*, vol. 10, no. 2, p. 187, Feb. 2023, doi: 10.3390/photonics10020187.

[13] D. Mulawa, "On-orbit geometric calibration of the OrbView-3 high resolution imaging satellite," *Int. Arch. Photogramm. Remote Sens. Spatial Inf. Sci.*, vol. 35, pp. 1–6, Aug. 2008.

[14] J. Wang et al., "The on-orbit calibration of geometric parameters of the Tian-Hui 1 (TH-1) satellite," *ISPRS J. Photogramm. Remote Sens.*, vol. 124, pp. 144–151, Feb. 2017, doi: 10.1016/j.isprsjprs.2017.01.003.

[15] B. Yang, Y. Pi, X. Li, and Y. Yang, "Integrated geometric self-calibration of stereo cameras onboard the ZiYuan-3 satellite," *ISPRS J. Photogramm. Remote Sens.*, vol. 162, pp. 173–183, Apr. 2020, doi: 10.1016/j.isprsjprs.2020.02.015.

[16] J. Cao et al., "In-orbit geometric calibration of HaiYang-1C coastal zone imager with multiple fields," *Opt. Exp.*, vol. 29, pp. 18950–18965, Jun. 2021, doi: 10.1364/OE.427023.

[17] Y. Zhang et al., "Accuracy evaluation on geolocation of the Chinese first polar microsatellite (ice pathfinder) imagery," *Remote Sens.*, vol. 13, no. 21, p. 4278, Oct. 2021, doi: 10.3390/rs13214278.

[18] L. Yang, X. Li, L. Jiang, F. Zeng, W. Pan, and F. Chen, "Resolution-normalizing image stitching for long-linear-array and wide-swath whiskbroom payloads," *IEEE Geosci. Remote Sens. Lett.*, vol. 19, pp. 1–5, 2022, doi: 10.1109/LGRS.2022.3201073.

[19] J. Li, Q. Hu, and M. Ai, "RIFT: Multi-modal image matching based on radiation-variation insensitive feature transform," *IEEE Trans. Image Process.*, vol. 29, pp. 3296–3310, Dec. 2020, doi: 10.1109/TIP.2019.2959244.

[20] A. Tommaselli and A. Berveglieri, "Automatic orientation of multi-scale terrestrial images for 3D reconstruction," *Remote Sens.*, vol. 6, no. 4, pp. 3020–3040, Apr. 2014, doi: 10.3390/rs6043020.

[21] X. Li, L. Yang, X. Su, Z. Hu, and F. Chen, "A correction method for thermal deformation positioning error of geostationary optical payloads," *IEEE Trans. Geosci. Remote Sens.*, vol. 57, no. 10, pp. 7986–7994, Oct. 2019, doi: 10.1109/TGRS.2019.2917716.

[22] M. Wang, Y. Cheng, B. Guo, and S. Jin, "Parameters determination and sensor correction method based on virtual CMOS with distortion for the GaoFen6 WFV camera," *ISPRS J. Photogramm. Remote Sens.*, vol. 156, pp. 51–62, Oct. 2019, doi: 10.1016/j.isprsjprs.2019.08.001.

[23] M. Wang, B. Yang, F. Hu, and X. Zang, "On-orbit geometric calibration model and its applications for high-resolution optical satellite imagery," *Remote Sens.*, vol. 6, no. 5, pp. 4391–4408, May 2014, doi: 10.3390/rs6054391.

[24] Y. Dong, D. Fan, Q. Ma, S. Ji, and H. Ouyang, "Automatic on-orbit geometric calibration framework for geostationary optical satellite imagery using open access data," *Int. J. Remote Sens.*, vol. 40, no. 16, pp. 6154–6184, Mar. 2019, doi: 10.1080/01431161.2019.1587206.

[25] S. Lee and D. Shin, "On-orbit camera misalignment estimation framework and its application to Earth observation satellite," *Remote Sens.*, vol. 7, no. 3, pp. 3320–3346, Mar. 2015, doi: 10.3390/rs70303320.

[26] Z. Guan, Y. Jiang, J. Wang, and G. Zhang, "Star-based calibration of the installation between the camera and star sensor of the Luojia 1–01 satellite," *Remote Sens.*, vol. 11, no. 18, p. 2081, Sep. 2019, doi: 10.3390/rs11182081.

[27] L. Jiang et al., "On-orbit geometric calibration from the relative motion of stars for geostationary cameras," *Sensors*, vol. 21, no. 19, p. 6668, Oct. 2021, doi: 10.3390/s21196668.

[28] D. Greslou et al., "Pleiades-HR innovative techniques for geometric image quality commissioning," *Int. Arch. Photogramm., Remote Sens. Spatial Inf. Sci.*, vol. 39, pp. 543–547, Aug./Sep. 2012.

[29] L. Lebègue et al., "Pleiades-HR image quality commissioning," *Int. Arch. Photogramm., Remote Sens. Spatial Inf. Sci.*, vol. 39, pp. 561–566, Jul. 2012.

[30] Y.-D. Pi, B. Yang, M. Wang, X. Li, Y.-F. Cheng, and W.-L. Tang, "On-orbit geometric calibration using a cross-image pair for the linear sensor aboard the agile optical satellite," *IEEE Geosci. Remote Sens. Lett.*, vol. 14, no. 7, pp. 1176–1180, Jul. 2017, doi: 10.1109/LGRS.2017.2702139.

[31] Y. D. Pi, B. Yang, X. Li, and M. Wang, "Study of full-link on-orbit geometric calibration using multi-attitude imaging with linear agile optical satellite," *Opt. Exp.*, vol. 27, no. 2, pp. 980–998, Jan. 2019, doi: 10.1364/OE.27.000980.

[32] G. Zhang, K. Xu, and W. Huang, "Auto-calibration of GF-1 WFV images using flat terrain," *ISPRS J. Photogramm. Remote Sens.*, vol. 134, pp. 59–69, Dec. 2017, doi: 10.1016/j.isprsjprs.2017.10.009.

[33] B. Yang, M. Wang, W. Xu, D. Li, J. Gong, and Y. Pi, "Large-scale block adjustment without use of ground control points based on the compensation of geometric calibration for ZY-3 images," *ISPRS J. Photogramm. Remote Sens.*, vol. 134, pp. 1–14, Dec. 2017, doi: 10.1016/j.isprsjprs.2017.10.013.

[34] Y. Jiang et al., "CCD distortion calibration without accurate ground control data for pushbroom satellites," *ISPRS J. Photogramm. Remote Sens.*, vol. 142, pp. 21–26, Aug. 2018, doi: 10.1016/j.isprsjprs.2018.05.008.

[35] H. Liu, D. Zeng, and Q. Tian, "Super-pixel cloud detection using hierarchical fusion CNN," in *Proc. IEEE 4th Int. Conf. Multimedia Big Data (BigMM)*, Sep. 2018, pp. 1–6, doi: 10.1109/BigMM.2018.8499091.

**Xiaoyan Li** received the B.S. degree in mechanism design, manufacturing and automatization from Northwest A&F University, Xi'an, China, in 2016, and the Ph.D. degree in circuit and system from the Shanghai Institute of Technical Physics of the Chinese Academy of Sciences, Shanghai, China, in 2021.

He is currently doing a Postdoctoral Research with the Hangzhou Institute for Advanced Study, University of Chinese Academy of Sciences, Hangzhou, China.

His research interests include on-orbit accurate navigation and geometric calibration of optical payloads, target detection, image processing, and machine learning.

**Liyuan Li** received the B.S. degree in optoelectronics information science and engineering from the Dalian University of Technology, Dalian, China, in 2018. She is currently pursuing the Ph.D. degree in physical electronics with the Shanghai Institute of Technical Physics of the Chinese Academy of Sciences, University of Chinese Academy of Sciences, Shanghai, China.

Her research interests include dim and small targets detection of IR through machine learning.

**Lixing Zhao** received the B.S. degree in intelligence science and technology from the Nanjing University of Science and Technology, Nanjing, China, in 2021. She is currently pursuing the M.A. degree in electronic information with the Hangzhou Institute for Advanced Study, University of Chinese Academy of Sciences, Hangzhou, China.

Her research interests include GCPs extraction for heterologous remote sensing images through deep learning.

**Jingjie Jiao** received the B.S. degree in electronic science and technology from Shandong University, Jinan, China, in 2021. He is currently pursuing the M.A. degree with the Hangzhou Institute for Advanced Study, University of Chinese Academy of Sciences, Hangzhou, China.

His research interests include satellite-borne SWaP cameras and test system for the infrared detectors.

**Linyi Jiang** received the B.S. degree in electronics and information technology program from Beijing Forestry University, Beijing, China, in 2018. She is currently pursuing the Ph.D. degree in electronic circuit and system with the Shanghai Institute of Technical Physics of the Chinese Academy of Sciences, University of Chinese Academy of Sciences, Beijing, China.

Her research interests include on-orbit geometric calibration of remote sensing satellites.

**Lan Yang** received the B.S. degree in mathematics and physics from Yunnan University, Yunnan, China, in 2019. She is currently pursuing the Ph.D. in physical electronics with the Shanghai Institute of Technical Physics of the Chinese Academy of Sciences, University of Chinese Academy of Sciences, Beijing, China.

Her research interests include on-orbit geometric calibration of satellite optical payloads, accurate navigation of remote sensing images, and image processing.

**Fansheng Chen** (Senior Member, IEEE) received the B.S. degree in optoelectronic information engineering from Shandong University, Jinan, China, in 2002, and the Ph.D. degree in physical electronics from the Shanghai Institute of Technical Physics of the Chinese Academy of Sciences, Shanghai, China, in 2007.

Since 2013, he has been a Professor with the Shanghai Institute of Technical Physics of the Chinese Academy of Sciences, Shanghai. His research interests include the design of spatial high-resolution remote sensing and detection payloads, high-speed and low-noise information acquisition technology, and infrared dim small target detection technology. Meanwhile, he has been committed to the research and development of space infrared staring detection instruments, high spatial and temporal resolution photoelectric payloads, and the application of infrared multispectral information acquisition technology in artificial intelligence, target recognition, and other relative aspects.

**Shengli Sun** is currently a Professor and the Director with the Shanghai Institute of Technical Physics, Chinese Academy of Sciences, Shanghai, China. His research interests include optoelectronic instrument design, space-based information acquisition and processing, and computer vision.